ACS APPLIED MATERIALS & INTERFACES

Research Article

www.acsami.org

Single Step Integration of ZnO Nano- and Microneedles in Si Trenches by Novel Flame Transport Approach: Whispering Gallery Modes and Photocatalytic Properties

Tim Reimer,[†] Ingo Paulowicz,[‡] Robert Röder,[§] Sören Kaps,[‡] Oleg Lupan,[‡,∥] Steffen Chemnitz,[†,⊥] Wolfgang Benecke,[⊥] Carsten Ronning,[§] Rainer Adelung,[‡] and Yogendra K. Mishra*[,‡]

[†]Technology for Silicon Based Micro- and Nanosystems, Institute for Electrical Engineering University of Kiel, Kaiserstr. 2, D-24143 Kiel, Germany

[‡]Institute for Materials Science, Functional Nanomaterials, University of Kiel, Kaiserstr. 2, D-24143 Kiel, Germany

[§]Institute of Solid State Physics, Friedrich-Schiller-University Jena, Max-Wien-Platz 1, 07743 Jena, Germany

[∥]Department of Microelectronics and Biomedical Engineering, Technical University of Moldova, 168 Stefan cel Mare Boulevard, MD-2004, Chisinau, Moldova

[⊥]Fraunhofer Institute for Silicon Technologies (ISIT), Fraunhoferstr. 1, 25524 Itzehoe, Germany

Supporting Information

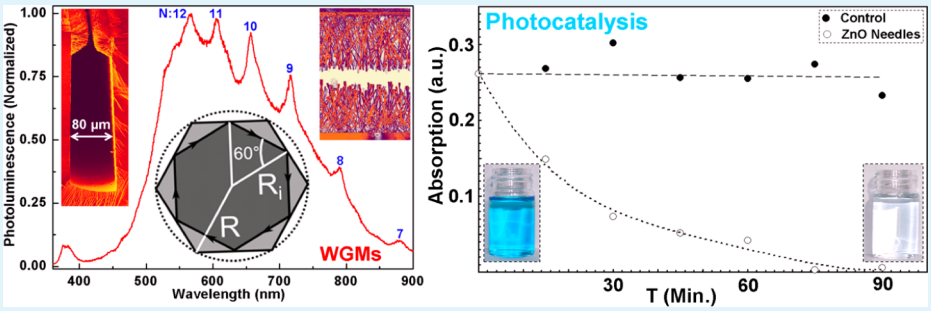

ABSTRACT: Direct growth of quasi-one-dimensional nano- and microstructures in desired places of complex shaped substrates using simple growth methods is highly demanded aspect for various applications. In this work, we have demonstrated direct integration of ZnO nano- and microneedles into Si trenches by a novel flame transport synthesis approach in a single fabrication step. Growth of partially and fully covered or filled trenches in Si substrate with ZnO nano- and microneedles has been investigated and is discussed here. Detailed microstructural studies revealed the evolution of the ZnO nano- and microneedles as well as their firm adhesion to the wall in the Si trenches. Micro-photoluminescence measurements at different locations along the length of needles confirmed the good crystalline quality and also the presence of whispering gallery mode resonances on the top of needles due to their hexagonal shape. Faceted ZnO nano- and microstructures are also very important candidates with regard to photocatalytic activity. First, photocatalytic measurements from the grown ZnO nano- and microneedles have shown strong degradation of methylene blue, which demonstrate that these structures can be of significant interest for photocatalysis and self-cleaning chromatography columns.

KEYWORDS: *ZnO, nano- and microneedles, flame transport synthesis, Si trenches, whispering gallery modes, photocatalysis*

1. INTRODUCTION

Quasi-one-dimensional (Q1D) metal oxide nano- and microstructures are currently under intensive investigation because of their extraordinary potentials for building real technological devices. Nanoscopic materials have been particularly interesting in the sense of excellent properties, but their integration into functional devices for real applications is still a challenging task. However, larger Q1D structures having intermediate dimensions in nano−micro scale are appropriate substitutes because they still exhibit desired nanoscale properties for advanced applications and they can be easily integrated to fabricate devices.

ZnO nano- and microstructures are one of the most investigated materials because of their versatile synthesis approaches for various applications ranging from nanoelectronic devices to biomedical engineering and environmental protection.[1−5] Due to its wide and direct bandgap ∼3.37 eV, large exciton binding energy ∼60 meV, hexagonal crystal structure with Zn and O terminated stacking along c-axis,[6] Q1D ZnO nanostructures have shown their potential for

Received: February 21, 2014
Accepted: April 28, 2014
Published: April 28, 2014

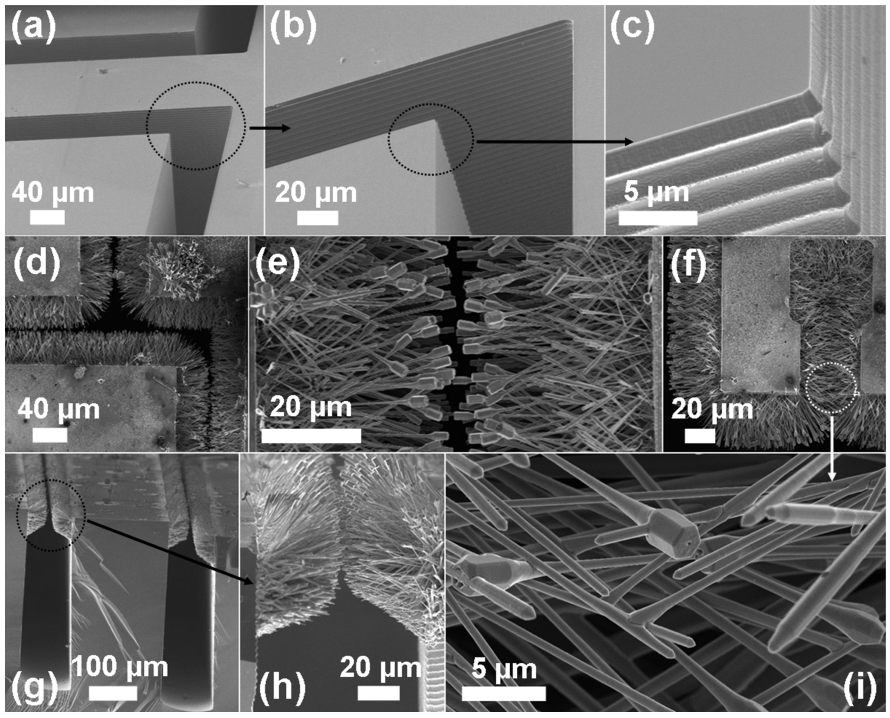

Figure 1. FTS grown needles inside a 80 μm wide trenches in Si substrate: (a–c) Zoom series of SEM images of the trenches (left to right) before ZnO structure growth. (d–f) SEM images of different ZnO nano- and microneedles grown at the edges of the trenches at different magnifications (top view). (g, h) Low and high magnification SEM images (cross-sectional view) from the ZnO needles grown in the trenches, respectively. (i) High magnification SEM image (top view) from the centre of trench (f) covered entirely with ZnO needles showing formation of interpenetrating junctions. The dotted circles correspond to the magnified regions from the sample in the SEM images.

optical, electronic and photonic applications, photodetectors, photodiodes, gas sensors, waveguides, solar cells, photocatalysts, etc.[7−13] Particularly in the context of the biomedical research, ZnO nanostructures exhibit antibacterial,[14] antiviral,[15,16] and anti-cancerous[17] properties, and they also have been regarded as biocompatible materials[18] but only up to certain doses because their size and shape dependent cytotoxicity starts playing a major role beyond the optimum conditions.[19]

ZnO structures can be hydrophilic or hydrophobic in nature depending on the number of vacant oxygen moieties on the surface. This property can be controlled by irradiating the structures with UV light and thus allowing a photoswitchable adjustment of wettability.[20] Based on attractive features for practical applications such as photocatalytic activity, sensoric devices, and switchable wettability, the ZnO structures might be suitable for micro-fluidics applications, for example, separating chemicals inside stationary chromatography columns. However, location specific growth of these Q1D ZnO nano- and microstructures (i.e., inside micro-channels on the Silicon chip) is the foremost requirement which must be fulfilled, and therefore, appropriate fabrication techniques are required. In addition to the aforementioned properties, hexagonal structures of ZnO can also be used as nanoscale whispering gallery mode (WGM) resonators.[21−25] In this application, ZnO provides higher quality factors and lower lasing threshold powers than lasers employing the classical resonator geometries and application of ZnO WGM lasers in the form of sensors has already been reported.[24] Therefore, these Q1D ZnO nano- and microneedles equipped with multifunctional properties such as whispering gallery modes, UV induced wettability, photocatalytic activity, etc. are of interest for various practical applications.

In the last decades, a significant understanding for growth procedures and application of ZnO nanostructures has been achieved, which makes it ready to be utilized in technologically relevant fields.[4,6,26,27] However, challenges for appropriate integration of nanostructures between electrodes on the chip or inside micro-channels in Si wafer hinder their application because of a lack of high quality contacts (both electrical and mechanical) between the nanostructures and the base material. In general, nanostructure based devices are built by multistep fabrication processes which on one hand do not assure the desired quality interface between nanostructure and electrodes and on the other hand the fabrication cost rises too high for the effective production at industry scale.

To overcome the nanodevice fabrication cost which rises too high and the contact issues, integration of Q1D nanostructures directly on silicon chips has been investigated extensively by using conventional methods such as vapor–liquid–solid process,[28,29] lithography,[30] electrochemical,[31] plasma,[32,33] flame-pyrolysis[34] etc. or by unconventional methods such as thin film fracture approach[35] and different devices have been fabricated but they include multistep processing. Recent progress in this regard suggests that slightly larger nanostructures, i.e., nano- and microstructures with at least one dimension in nanoscopic range, would be preferable as they can be easily handled and a direct growth method is available which allows integrating these nano-microstructures in a single fabrication step.[36,37]

As already mentioned, there are several fabrication methods available in literature but desired growth of nano-microstructures directly in micro-channels is still an open issue.

There exist only a few reports that have described direct growth of Q1D ZnO nanostructures on chips using different methods but most of them involve multiple fabrication steps.[38−40] The potential of the newly introduced flame transport synthesis (FTS) technique,[41] which is a very simple fabrication approach for hexagonal ZnO nano- and microstructures, is great for micro-trenched Si wafers due to a cost effective and single-step process.[15,16,42]

In this study, we have investigated ZnO nano- and microneedles integrated directly in Si trenches on wafer using novel single step flame transport synthesis as advanced photocatalytic and optical materials. Developed approach allows a simpler fabrication of hexagonal ZnO nano- and microneedles on micro-trenched Si wafer in a very cost effective and single-step process. Detailed structural and optical studies of hexagonal ZnO nano- and microneedles grown inside micro-channels are elaborated for the first time. Additionally, the photocatalytic activity of the nano- and microneedles is presented, which suggests that our structures could be used in photocatalytic applications.

2. EXPERIMENTAL SECTION

2.1. Fabrication of Trench Wafer. Single side polished 200 mm in diameter ⟨100⟩-silicon wafers served as substrates to create up to 400 μm deep trenches with micro system technologies (Bosch process).[43] The wafers were patterned with suitable test structures in a single lithography step utilizing the photoresist OIR908-35 Fujifilm with a thickness of 4.3 μm and a Canon stepper FPA3000iw. Developed regions remain unmasked and were exposed to a subsequent dry etch step. Deep reactive ion etching on a STS Pegasus tool has been used to achieve vertical sidewalls. This anisotropic etching consists of an alternating procedure by depositing a protective polymer on the sidewalls and isotropic etching of the trench bottom. Cycling of both results in the final etch depth while the process parameters control the etch rate, uniformity, tilt, and scallops of the fabricated trenches. Scallops (often referred as sidewall roughness and shown in Figure 1c) are the thickness of a single cycle and are measured on the sidewall; they decrease as etch progresses. In the process used here, a 4 s long deposition (protective polymer) at 35 mTorr with 250 sccm C_4F_8 and 2500 W coil power has been applied, the etching parameters were 150 mTorr, 750 sccm SF_6, an 45 sccm O_2 at 3500 W coil power and 30 W platen power for 8 s. The overall etch rate depends on the trenches' aspect ratio, for the 80 μm wide trenches here 7.0 μm has been achieved.

2.2. Growth of ZnO Nano- and Microstructures. The silicon substrates with trenches were used as substrates for growth of ZnO nano- and microneedles in a controlled variant of the FTS approach.[41] The crucible was filled (∼60% by volume) with Zn microparticles (diameter ∼ 5 μm from GoodFellow, U.K.) and polyvinylbutyral (PVB) sacrificial polymer powder (Mowital B 60H from Kuraray GmbH, Europe) in the ratio of 1:2. The Si substrate was mounted on the top of the crucible with the trenches facing towards the crucible holding the precursor powder mixture. The whole arrangement was then inserted into the muffle type oven (Supporting Information, Figure S1) and it was heated to 900 °C for 30 min and afterwards was allowed to cool naturally. The FTS process leads to the growth of different ZnO nano- and microneedles and the specimen were ready for further characterization.[41]

2.3. Characterizations. The morphologies of nano- and microneedles were investigated using scanning electron microscopy (SEM) instruments, Dualbeam Helios Nanolab (FEI) (20 kV, 20 μA) and Zeiss Ultraplus (3 kV, 15 μA). X-ray diffraction (XRD) studies were performed by using XRD 3000 Pts Seifert system (with 40 kV and 40 mA, Cu Kα_1 radiation with λ = 0.1541 nm). The average crystal lattice parameters were determined by the Scherrer method from the diffraction peaks. Raman scattering measurements were carried out with a WITec LabRam Alpha 300 system in a backscattering configuration. A 532.2 nm line of Nd-YAG laser was used for off-resonance excitation with less than 4 mW power at the sample. Room temperature micro-photoluminescence (μPL) measurements at different positions on these ZnO nano- and microneedles in the trenches were performed using a home-built far-field epifluorescence microscope.[44] The HeCd laser beam (325 nm, cw) was focussed on the specimen with a spot size of 15 μm^2 by a reflective objective (36×, NA = 0.5) as well as white light for microscopic observation. With this spot size, a superposition of typical ∼4−10 nano- and microneedles was measured. The luminescence light of these needles was collected by the same objective, dispersed by a 500 mm monochromator (spectral resolution of ∼0.7 nm) and detected by a nitrogen cooled charge-coupled device (CCD). The entry slit of the monochromator and CCD detection lines were chosen that way to measure likely only the luminescence from the excitation spot.

2.4. Photocatalytic Measurements. The photocatalytic properties of these structures were investigated by immersing the Si substrate with ZnO needles in a solution of 1 μmol L^{-1} methylene blue (MB) and irradiating with UV light for 90 min. A magnetic stirrer was used to stir the liquid at 300 rpm. A self-made device from stainless steel and Teflon was used to mount the sample and adjust the height (∼10 mm) of the sample in such a way that magnetic stirrer can move freely. A locally produced UV diode array consisting of 4 diodes (central wavelength = 370 nm, 170 mW per diode) was mounted at about ∼13.5 cm above the sample for illumination. The MB solution was prepared from a 1 m-mol L^{-1} stock solution. Stock solution (100 μL) was taken by Eppendorf Pipette and pipetted into a volumetric flask, and then, the flask was filled to 100 ml with distilled water. Aliquots of the solution (∼1 ml each) were taken after 0, 15, 30, 45, 60, 75, and 90 min of the photocatalytic treatment to observe the change in concentration. Aliquots were pipetted directly into precision glass cuvettes (Hellma Analytics, 10 mm path length), and absorption was measured. Glass cuvettes were cleaned by careful rinsing with deionized water and isopropyl alcohol after each measurement and then allowed to dry. Sample concentration was investigated using photometry, employing a UV−vis spectrophotometer (Perkin Elmer, UV/Vis/NIR Spectrometer Lambda 900). The highest intensity signal for MB at a wavelength of 664 nm was employed for determining the relative concentration. A reference sample was treated as described above but without the Si/ZnO sample or the stainless steel/Teflon mounting.

3. RESULTS AND DISCUSSION

Figure 1 shows SEM images from the Silicon substrates having trenches and the grown ZnO nano- and microneedles by the FTS approach. The trenches (∼80 μm wide and ∼300 μm deep) were grown in Si using the Bosch etching process.[43] The detailed SEM investigations on trenches in Si have been performed and a zoom series of SEM images of two neighbouring trenches is presented in Figure 1(a−c) with increasing order of magnifications (a−c). A high magnification SEM image corresponding to a trench from Figure 1a is shown in part b, which reveals the perfect corners of the trench on the top and the presence of wrinkles on the walls of the trenches. Surfaces having wrinkles in particular are highly preferable for favorable growth or smart adhesion as compared to smooth ones.[45] An even higher magnification SEM image from the corner of the trench shows that wrinkles have average lambda (λ) value about ∼3.3 μm and height around 1.4 μm. Figure 1(d) shows the top view SEM image of ZnO nano- and microneedles grown along the trench. It can be seen that these needles start to grow on both sides perpendicular to the surface of the trench wall and their lengths can be controlled by different growth parameters. Since ZnO needles grow from both sides within the trench, they can easily cover the entire top surface of the trench and depending upon the requirement, it can be controlled. Figure 1e shows the top view SEM image

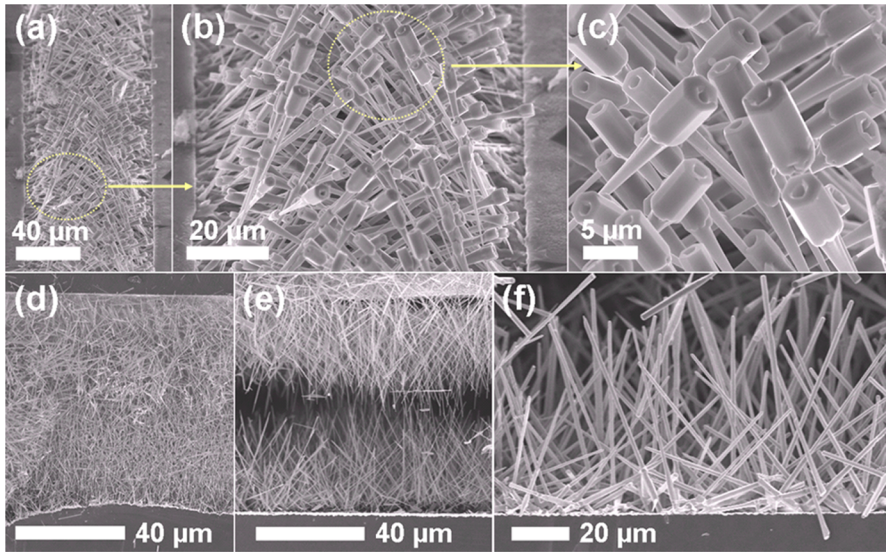

Figure 2. SEM images (top view) of the grown ZnO nano- and microneedles and wires in the trenches by the FTS approach. (a–c) Zoom series of SEM images from trench entirely covered with ZnO nano- and microneedles. The high magnification SEM image in part c shows the cross-entanglements between the nano- and microneedles. The dotted circles in (a, b) correspond to the magnified regions in the SEM images. (d–f) SEM images from trench grown with ZnO nanowires: (d) Trench entirely covered with ZnO nanowires. (e) Partially covered trench with ZnO nanowires. (f) High magnification of image in part e, demonstrating the dimension of the Q1D wires and the wrinkled surface of trenched Si wall.

from a trench where ZnO nano- and microneedles are approaching to cover the gap of the trench. A further SEM image (top view) from a trench, which is entirely covered with ZnO nano-and microneedles is presented in Figure 1f. These 'nano- and microneedles' are very thin (~100–200 nm) at the base and thicker (~1 μm) on the top. From the geometrical aspect, they exhibit a long conical base with a hexagonal tip at the end. In this case, the ZnO needles grow from both sides in the trench and cover the entire opening area of the trench.

To investigate further, whether the ZnO nano- and microneedles grow up to entire depth of the trench or only up to certain depth, side view SEM measurements along the depth of the trench have been performed and are shown in Figure 1, g and h, respectively. It is clear from Figure 1g that these needles grow mainly on the top-edge corners entirely along the trench length but only grow up to certain depths inside the trench. Nano- and microneedles located near the top edge of the trench wall exhibit maximum lengths, but at lower locations of the wall along the depth of the trench, their length decreases and there is almost no nanoneedle growth beyond a depth of ~40–50 μm as revealed by high magnification SEM image shown in Figure 1h. This confirmed that the ZnO nano- and microneedles mainly grow as shades on the top edge to cover the trench opening but the underneath space in the trench remains unoccupied. To further demonstrate the ZnO needles shade, SEM measurements of a typical trench entirely covered with such needles were performed and a higher magnification image is shown in Figure 1i. It is found that these needles grow perpendicular to both edges (top) of the trench to shade the trench's gap join together and forming interpenetrations between them. With further increase in time, the nanoscopic ZnO needles interpenetrate each other and their growth is further continued along the c-axis. Partially and entirely shaded trenches with Q1D ZnO needles have been grown (Supporting Information, Figure S2).

Different types of Q1D ZnO nano- and microneedles on the edge of trenches can be grown by the FTS method. For example a zoom-in series (left to right) of SEM images from a trench entirely covered with inter-bridging ZnO nano- and microneedles is shown in Figure 2a–c. These needles exhibit hollow hexagonal tips supported by a long conical base attached to the trench wall. A corresponding high magnification SEM image shown in Figure 2c demonstrates crossing needles with clearly visible holes in their hexagonal tips. Formation of these holes on the hexagonal is most likely due to re-evaporation of ZnO at high temperatures during growth process (see Supporting Information, Figure S2e). More details on this topic will be presented in a forthcoming work. Another example of ZnO nanowire shade covering the entire trench opening is shown by top view SEM image in Figure 2d. It can be observed that the ZnO nanowires interconnect in a hierarchical manner within the shade. Figure 2e shows the SEM image (top view) from the trench where ZnO nanowires are approaching towards each other to bridge the trench gap. Further high magnification SEM image in Figure 2f from the trench-edge shows the wrinkled Si surface and the grown ZnO nanowires on the trench edge. Most of these ZnO nanowires grow vertically on the surface of trench wall, but their directions are X-type oriented.

In order to understand the growth mechanism of these Q1D ZnO nano- and microstructures, detailed SEM investigations at the ZnO/Si interface (i.e., on the trench wall) were performed and corresponding SEM observations are shown in Figure 3a–c. A suitable location where only few ZnO nanowire grown on the surface of the trench was selected for a better imaging and supporting growth mechanism. The SEM image in Figure 3a demonstrates that these nanowires grow in X-type orientation on the surface of the Si trench. The high resolution SEM image from the base of one of these ZnO wires (Figure 3a) is shown in Figure 3b, which confirms that these ZnO nanowires exhibit the hexagonal base. After a careful look at the nanowire base in Figure 3c, one can realize the difference in contrasts between Si surface (underneath) and the layer at the nanowire base; it seems that an additional layer of ZnO as interface is also grown at the trench's surface. To further confirm the interface layer, a

dx.doi.org/10.1021/am5010877 | ACS Appl. Mater. Interfaces 2014, 6, 7806–7815

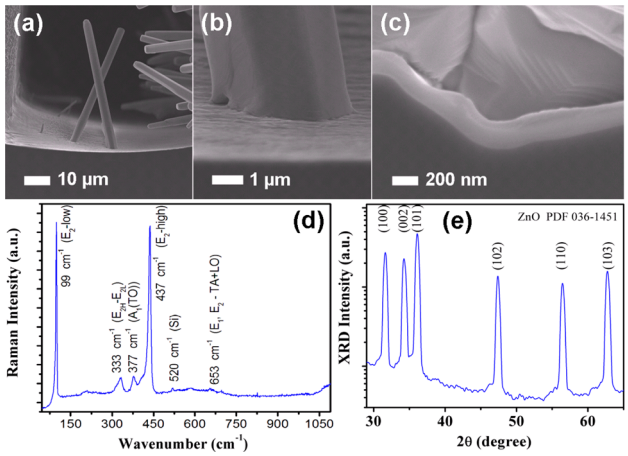

Figure 3. High magnification SEM investigation for the Si/ZnO interface: (a) SEM image of two vertically standing ZnO wires on the etched surface. (b) High magnification SEM image from the base of ZnO wire on etched Si surface. (c) Further high magnification SEM image from another Si/ZnO interface showing the formation of thin (~200 nm ZnO) layer on etched Si surface. (d) Typical Raman spectrum of grown ZnO nano- and microstructures in the Si trench. (e) X-ray diffraction spectrum from ZnO nano- and microneedles in the trench on Si substrate.

separate location was analyzed where Si wrinkles can be clearly observed in a high magnification SEM image (Figure 3c).

The dark contrast from the Si wrinkle and the bright contrast from the grown ZnO layer (~200 nm thick) at the interface between ZnO nanowire and surface of trench can be clearly distinguished. The high resolution SEM studies at the interface also confirmed the formation of intimate contact (Supporting Information, Figure S3) between ZnO nano- and microneedles and Si substrate and thus these needles exhibit a very good adhesion to the substrate surface, which is in general a highly demanded aspect for various applications.

Growth of such type of ZnO nano- and microneedles on a trench wall in the flame transport synthesis approach occurs in a unique manner. The Si substrate patterned with trenches was mounted as the top cover on the ceramic crucible (see Supporting Information, Figure S1) which was filled with about ~60–70% of a mixture of precursor Zn microparticles and sacrificial polymer (PVB).[41] The heating process generates intense flame from the crucible due to rapid burning of PVB. Because of the upward flame stream and its high temperature, the precursor Zn microparticles were transported and simultaneously converted into Zn atomic vapor, which is then reaching the substrate's surface having trenches. The PVB generated flame also provides necessary oxygen control for the ZnO nano- and microneedles growth. The furnace has a three dimensional temperature profile, and thus, the substrate was also hot equivalently to the furnace temperature. The arriving Zn and O atoms were deposited into the trenches in form of a very thin ZnO layer (~200 nm), which serves as nucleation centres for further arriving Zn and O atoms and possibly for very small ZnO nanostructures too. According to our experimental observations, the surface morphology of the trench plays a very important role in the growth because it guides the initial growth of thin ZnO layer, which creates the nucleation sites for growth of high crystal quality hexagonal ZnO nano- and microneedles.

Apart from surface quality, the aspect ratio (width to depth) and shape (U or V type) of trench are equally important parameters for the growth of nano- and microneedles. In trenches with higher aspect ratio, growth of ZnO nano- and microneedles mainly occurs in the top regions (near edges) of the trench walls; however, for trenches with lower aspect ratios (i.e., trenches having large widths), growth over entire trench surface can take place. The SEM observations suggest that in V-shaped trench, needles growth will occur down to higher depths, because in V-shaped trench relatively large area is facing towards the crucible consisting of precursor material.

Here, we have demonstrated only the growth of different Q1D ZnO nano- and microstructures in U shaped trenches (width ~80 μm and depth ~400 μm) in Si created by the Bosch etching process.[43] Since the width of the trench is relatively small (~80 μm), ZnO nano- and microneedles mainly grow on the top edge of the trench; however, the underneath space remains empty (Figure 1g and h). Growth of Q1D ZnO nano- and microneedles predominantly starts perpendicularly at the edges on both sides of the trench's wall with the tendency to form bridges across the trench gap (Figures 1d–i and 2a–e). Apart from trench dimensions and shape, experimental parameters such as amount of precursor material, height and opening of the crucible, processing temperature, and time strongly influence the nanostructures growth in the trench. Depending upon the requirements, the trench opening can be partially or entirely shaded with Q1D ZnO nano-and microneedles by controlling different parameters. The trenches partially covered with FTS grown ZnO nano- and microneedles are shown in Figure 1d–e and g–h, and a fully covered trench with interpenetrating ZnO needles is shown by SEM image in Figure 1f and corresponding high magnification SEM image in Figure 1i, respectively. It can be seen that ZnO nano- and microneedles partially or completely interpenetrate each other (Figure 1i). An example where the trench gap is entirely covered with entangled hexagonal ZnO needles is demonstrated by the zoom series (left to right) of SEM images in Figure 2a–c. The ZnO nano- and microneedles in the present case are thinner at the base and thicker at the top with a hexagonal tip which is hollow (Figure 2c).

As already mentioned, during the FTS process, the initially arrived Zn, O species form a thin layer on the trench's surface, which then provides nucleation sites for growth of ZnO nano- and microneedles. After the nucleation process, the arriving Zn, O atomic and molecular species find these nucleation sites to be energetically favorable locations and thus contribute in further growth of ZnO needles along c-axis. With respect to time, the arriving atomic and molecular species are preferably deposited on the top of growing needles rather than reaching down to their base. The probability for arriving species to reaching down to the base decreases with increase in the length of nano- and microneedles, because before reaching to the base, there are high chances that they are captured by neighboring needles. This is also a main factor responsible for nano- and microneedles to be thinner at the base and thicker at their heads. The ends of the nano-and microneedles acquire hexagonal shape in the final growth stage, which is the most energetically favorable state for the case of ZnO structures.

In order to investigate the structural quality of these FTS grown ZnO nano- and microneedles in the trenches, detailed Raman measurements at different locations in the trenches have been performed and a typical optical-phonon spectrum is shown in Figure 3d. In all the measurements, the incident laser

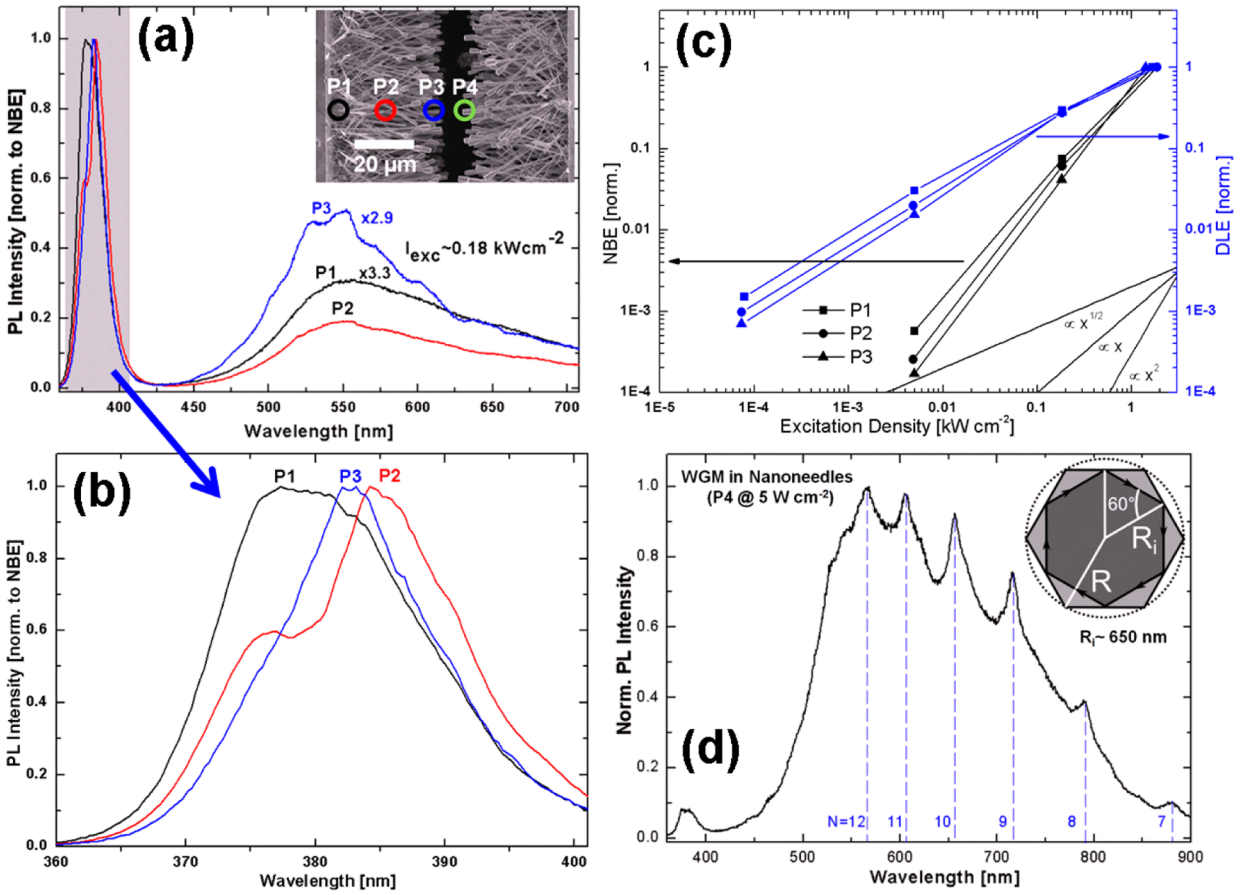

Figure 4. (a) Room temperature photoluminescence spectra corresponding to locations P1 (base), P2 (middle), and P3 (tip) on ZnO nano- and microneedles in the trench on Si wafer. The inset in part a shows the SEM image of ZnO nano- and microneedles and corresponding locations (P1, P2, and P3) where PL measurement spectra have been obtained. (b) Magnified NBE spectra corresponding to marked region in part a with respect to locations P1, P2, and P3. (c) Variation in integrated NBE (black) and DLE (blue) PL intensities as a function of excitation density for corresponding measurements at locations P1, P2, and P3. (d) PL spectrum from the top of the needles (location P4 in the inset of part a) where laser beam mainly falls on hexagonal portion of the needle. Along with inherent blue NBE and green DLE emission, appearance of WGM due to hexagonal geometry can also be observed. The inset in part d shows the typical dimensions used for simulating different WGMs in the PL spectra corresponding to location P4 in the trench. The PL spectrum in part d was acquired with about 40 times weaker optical excitation than the spectra in part a. This further demonstrates the sensitivity of the NBE/DLE ratio as a function of optical excitation in part c, which is caused by the saturation of the defect band emission.

light was always perpendicular to the ZnO nano- and microstructures and the Raman signal was recorded in the backscattering geometry. Wurtzite ZnO belongs to the C_{6v}^4 space group $P6_3mc$, and the primitive cell contains two formula units with all atoms on 2*b* lattice sites having C_{3v} symmetry. The normal lattice vibration modes from ZnO at the Γ point of the Brillouin zone can be predicted by group theory (eq 1)[31] as

$$\Gamma_{opt} = A_1 + 2B_1 + E_1 + 2E_2 \quad (1)$$

Raman scattering is mainly governed by the polarization dependent selection rules imposed by the crystal symmetry. Non-polar optical phonon modes with symmetry E_2 have two frequencies: high (E_{2high}) and low (E_{2low}) frequency phonons. The E_{2high} mode is associated with the oxygen atoms; however, the E_{2low} mode is associated with the vibration of the heavy Zn sublattice. The B_1 modes are silent, and the others are Raman active. Raman modes A_1 and E_1 are polar, infrared active and split into the transverse optical (TO) and longitudinal optical (LO) phonon modes. All peaks in Raman spectrum shown in Figure 3d corresponding to ZnO nano- and microneedles are referred to a wurtzite ZnO structure according to previous reports.[12,46]

The two strong vibration peaks at 99 and at 437 cm^{-1} are assigned to the two nonpolar optical phonon (E_2) modes of ZnO at low and high frequencies, respectively. The other very intensive Raman mode in ZnO is E_{2high} ~ 437 cm^{-1}, dominantly assigned to oxygen vibrations.[47] It is very intensive and exhibits a full width at half-maximum of about 11 cm^{-1}, which further confirms that nanoneedles are made of high quality hexagonal wurtzite structure. The asymmetry of the peak E_{2high} on the left-hand side of mode is due to presence of the E_1(TO) mode at 411 cm^{-1}. The peaks at about 378 cm^{-1} and 580 cm^{-1} correspond to the polar transverse A_1(TO) mode and the longitudinal E_1(LO) optical phonon mode, respectively. Other modes with frequencies of 333, 541, 661, and 1147 cm^{-1} corresponds to bulk phonon modes and the are attributed to multiphonon scattering processes.[12,47] The Raman peak at 333 cm^{-1} is attributed to the second order Raman processes from zone-boundary phonons E_{2high}−E_{2low} mode.[47] The peaks at 541 and 661 cm^{-1} are attributed to 2−LA and TA +LO combinations at the *M* point, respectively. In addition, the 1147 cm^{-1} mode may be attributed to 2−LA overtones along

dx.doi.org/10.1021/am5010877 | ACS Appl. Mater. Interfaces 2014, 6, 7806−7815

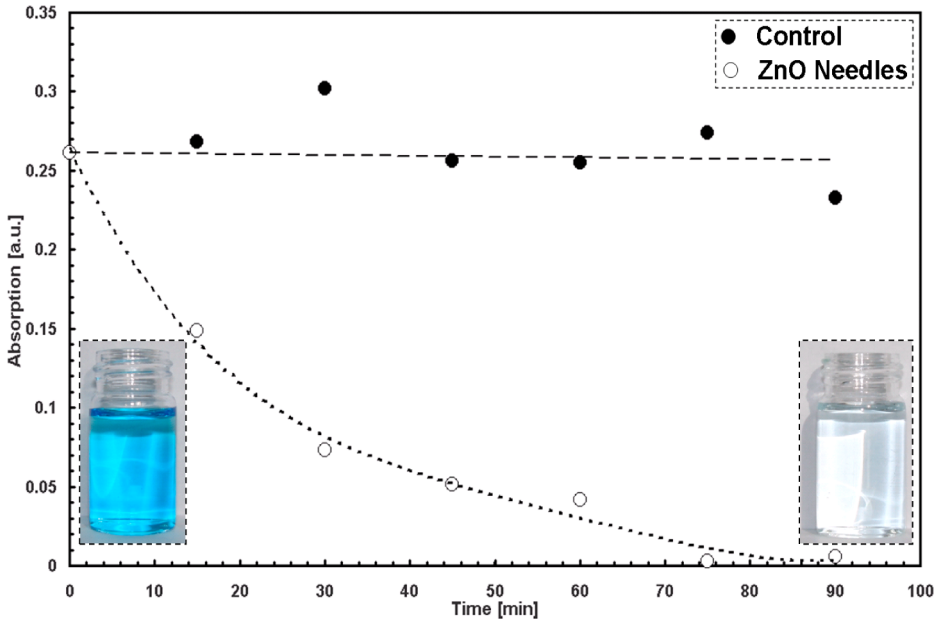

Figure 5. Photocatalytic activity of the grown ZnO nano- and microneedles for a period of 90 min. The ZnO nano- and microneedles show a significant decrease in the concentration of MB dye in comparison to control sample (without ZnO). The inset images show the colour of aqueous MB solution, before (left) and after 90 min of degradation by ZnO nano-microneedles (right).

A−*L* and *M*. No LO-phonon peaks are seen in the spectrum of ZnO, because the incident light is perpendicular to the *c* axis of wurtzite ZnO. The peak at 520 cm^{-1} corresponds to Raman signal from the silicon substrate because of the penetration of the excitation laser light.

In order to assure the high crystalline nature, X-ray diffraction measurements of fabricated ZnO nano- and microstructures in the trenches were performed, which further confirm their hexagonal wurtzite crystal structure. A typical XRD pattern from ZnO nano- and microstructures in the trench is shown in Figure 3e, which reveals that these ZnO structures do not exhibit a dominant reflection or a preferential growth with respect to the substrate. The main XRD peaks are (100), (002), and (101) from these samples. Similar to Raman, XRD measurements at different locations have been performed and all of them showed almost identical XRD pattern. The narrow FWHM values in the XRD peaks reveal that the synthesized ZnO nano- and microstructures are of high crystal quality. The lattice parameter $d_{(002)}$ in the unstressed ZnO bulk is about 2.602 Å; however, the calculated one is about 2.608 Å for the synthesized ZnO structures, which also confirms their high crystalline quality[48,49] and indicates a low strain level that exists in nanowires.

Detailed room temperature micro-photoluminescence (μ-PL) studies on ZnO nano- and microneedles grown in the trenches have been performed and results corresponding to one representative trench are demonstrated in Figure 4. Micro-PL measurements were performed at different locations (P1, P2, and P3) on the ZnO nano- and microneedles with different laser excitation intensities (I_{exc}) to gain also the power dependent information. Figure 4a shows the room temperature PL spectra from locations P1, P2, and P3 (according to the SEM image shown as inset) at a constant excitation density of ~0.18 kW/cm^2. The PL intensity is most intense for P2 but in general of the same order for all positions with respect to measurement deviations such as excitation volume, number of measured needles, and scattering. The near band edge (NBE) emission, which is typically caused by excitonic recombinations is spectrally located around ~380 nm.[24,42] The deep level defect luminescence (DLE) known as green luminescence of ZnO, causes a broad emission band between 450 and 700 nm. The DLE at comparable excitation conditions is relatively to the NBE most intense at P3 and least intense at P2. The more intense DLE at P3 might be caused by the larger excitable volume at the hexagonal tips leading to higher number of contributing defects, although the defect density should be at least as low as at P2 and P1, as indicated by the saturation of the DLE in the power dependent measurement in Figure 4c and Supporting Information, Figure S4. The nano- and microneedles exhibit slightly higher defect concentrations at their bottoms (P1) close to the substrate compared to P2. The crystalline quality might therefore be lower at the base (location P1) due to the initial growth. The NBE shows furthermore a more complex structure depending on the position shown in Figure 4b: first emission band around ~376 nm and second emission around ~383 nm. The observed red-shift in the NBE spectrum might be related to the growth, because the band at the low energy side gets more dominant at comparable excitation powers, when the excitation spot is moved from P1 over P2 to P3. The energetic difference between these both NBE bands accompanied by the nearly quadratic power dependence of the NBE in Figure 4c, which is dominated by the 383 nm band at increased excitation, gives rise to the assumption that the low energy band might be caused by the nonlinear exciton−exciton scattering usually labeled P-band.

Figure 4c shows the integrated NBE (black) and DLE (blue) PL intensities as a function of excitation density (I_{exc}) corresponding to locations P1, P2, and P3 on the ZnO needles. The DLE (460-650 nm) clearly exhibits a sub-linear dependence with excitation density I_{exc}, which indicates the saturation behavior. The saturation behavior of the defect driven luminescence (DLE) is a very good hint for the rather good optical quality of the nano- and microneedles. The evolution at all positions seems to be comparable. The

hexagonal top ends of the needles especially at locations P3 and P4 exhibit furthermore suitable resonator morphologies to show excellent whispering gallery modes,[21] although a hollow hexagonal resonator structure is present. The optical mode seems therefore not to be extremely distorted or affected by the hole. The estimation of possible propagating transverse TM modes for a single hexagon with an inner radius $R_i \sim 650$ nm fits nicely the emission spectrum at P4 in Figure 4d. The inner radius is in good agreement with the measured values from SEM investigations.[21] Also the PL emission detected from P3 shows WGMs, but here, it is difficult to assign each single mode due to the superimposition of emissions originating from different needles. Whispering gallery modes at several locations where ZnO needles exhibit hexagonal shapes have been found and also signatures of waveguide effects during Raman as well as PL measurements have been observed. Whispering gallery modes were not observed superimposed to the NBE, since the modes get closer in the spectral region of the NBE and only 2−3 modes with WGM numbers N above 20 would fit under the envelope of the NBE. Assuming furthermore a low Q-factor, any present WGMs could hardly be distinguished in reasonable signal acquisition times, as they have to be above noise intensity.

Enhancing the photocatalytic activity of different ZnO nano- and microstructures has been a focused issue for various applications in chemistry.[50−57] According to previous reports, it has been observed that the photocatalytic behavior of ZnO nanostructures is almost independent on their size; however, their aspect ratios show major contributions towards photocatalytic activities.[57] Faceted and polar surfaces are quite important in this regard as they are helpful in separating the photogenerated electron−hole (e−h) pairs (i.e., preventing from spontaneous e−h recombination) and thus provide an increased photocatalytic activity. Hexagonal faceted ZnO rods have shown at least 5 times higher photocatalytic activity in comparison to nanorods with smooth surfaces.[55] It has also been demonstrated that by tuning the face orientations of ZnO nano- and microstructures, their photocatalytic response can be optimized.[51] Thus, ZnO nano- and microstructures exhibiting different facets are very important candidates with regard to photocatalytic applications. Since the ZnO nano- and microneedles in the present case are directly integrated into the walls of trenches and their surface is smooth at the bottom and hexagonally faceted at the top, they can be directly utilized for different chemistry applications (e.g., separating chemicals etc.). However, their photocatalytic properties are equally important which has been tested with respect to methylene blue (MB) and the corresponding results are shown in Figure 5. The experimental curve demonstrates that a quick decrease in MB concentration occurs due to the ZnO nano- and microneedles present in the microtrenches, in comparison to a control sample (under identical conditions). The promising photocatalytic activity displayed by our nano- and microneedles could be very helpful for various applications in the field of microfluidics. The samples tested in this paper showed a photocatalytic activity that appears to be comparable to that of metal-coated ZnO, reported elsewhere.[58] The results also appear comparable in magnitude to photocatalytic activity of ZnO nanowires grown by carbothermal reduction process.[59] However, in our case, the ZnO has the advantage of having been grown directly in trenches, improving the potential for direct application as a photocatalytic material in microfluidic reaction devices. It is very important to emphasize here that conventional freestanding ZnO nanostructures (e.g., nanoparticles, nanorods etc.) might have better photocatalytic activities but their integration into the trenches is even more challenging task. These integrated ZnO nano- and microneedles exhibit the advantage that their photocatalytic behavior can be conveniently utilized, and they are also available for multiple uses.

It is also clearly visible that even a small amount of these ZnO nano- and microneedles on Si substrate is enough to express strong photocatalytic activity, as dye concentration was reduced to almost zero after 90 min of UV irradiation, while the control sample clearly retained its original dye content. The change in color of MB solution after degradation to ZnO nano- and microneedles is clearly visible by naked eye (insets in Figure 5). The preliminary photocatalytic result shows that these grown nano- and microneedles could be of use in self-cleaning lab-on-a-chip liquid chromatography applications and further experiments in this regard are already under progress. For example, a lab-on-a-chip microchromatography device could be constructed by bonding a Si/ZnO microfluidics wafer with a glass top wafer. A UV diode can be easily fitted above the glass wafer, so that its light could cause photocatalytic decomposition of pollutants after a successful use of the device for substance separation.

4. CONCLUSIONS

In this work, we have demonstrated the versatile growth of ZnO nano- and microneedles directly on the surface of the Si trench wall by using a single step process by simple flame transport synthesis approach. The aerial growth of ZnO nano- and microneedles on the surface of the Si trench mainly depends on its aspect ratio. For trenches with lower aspect ratio, growth of structures occurs over larger surface of the trench wall; however, it mainly occurs on top edges for trenches having large aspect ratio. Growth of ZnO nano- and microneedles on the top edges of the trenches with partially as well as fully shading is shown. It was observed that the ZnO needles are thinner at the base and get thicker on top as they grow perpendicularly along the surface of the trench and at the end they exhibit hexagonal cylindrical tips. The FTS grown ZnO needles are of high crystalline quality as confirmed by X-ray diffraction, micro-Raman spectroscopy, and photoluminescence spectroscopy investigations. Detailed micro-photoluminescence studies revealed the presence of excellent whispering gallery modes due to hexagonal resonator shape of ZnO needles in the centre of the trench which might be of significant interest for advanced optical applications. The grown ZnO nano- and microneedles with hexagonal facets also showed strong photocatalytic activity with respect to methylene blue dye. Therefore, such type of Q1D ZnO nano- and microneedles grown in the trenches with multifunctional properties such as whispering gallery resonances and strong photocatalytic response could be promising candidates for applications in the direction of confined light guiding or separating chemicals in chromatography columns. Our results are also very important for further investigations on self-cleaning microfluidics devices, microfluidic photoreactions, and similar topics.

■ ASSOCIATED CONTENT

Supporting Information

Schematic graphic of the experimental setup (Figure S1); additional high magnification SEM images of ZnO needles from different regions of the trenches (Figure S2); detailed high

magnification studies of the interface between ZnO needles and silicon substrate (Figure S3); variation in the ratio of integrated NBE to DLE intensities as a function of excitation density, indicating the saturation behavior of the DLE (Figure S4). This material is available free of charge via the Internet at http://pubs.acs.org/.

AUTHOR INFORMATION

Corresponding Author

*Email: ykm@tf.uni-kiel.de.

Notes

The authors declare no competing financial interest.

ACKNOWLEDGMENTS

Authors thank the financial support from Fraunhofer Institute for Silicon Technology, Itzehoe, Germany. Y.K.M. and O.L. acknowledge the Alexander von Humboldt Foundation for the financial support through research fellowships at the Institute for Materials Science, University of Kiel, Germany. This research was sponsored by the German Research Foundation (DFG) under the schemes SFB 855-A5, FOR 1616, and, partially, SFB 677-C10. Furthermore we are grateful to EU-Graphene Flagship for the financial support.

REFERENCES

(1) Xia, Y.; Yang, P.; Sun, Y.; Wu, Y.; Mayers, B.; Gates, B.; Yin, Y.; Kim, F.; Yan, H. One-Dimensional Nanostructures: Synthesis, Characterization, and Applications. *Adv. Mater.* **2003**, *15*, 353−389.

(2) Vaseashta, A.; Vaclavikova, M.; Vaseashta, S.; Gallios, G.; Roy, P.; Pummakarnchana, O. Nanostructures in Environmental Pollution Detection, Monitoring, and Remediation. *Sci. Technol. Adv. Mater.* **2007**, *8*, 47−59.

(3) Masciangioli, T.; Zhang, W.-X. Environmental Technologies at the Nanoscale. *Environ. Sci. Technol.* **2003**, *37*, 102A−108A.

(4) Wang, Z. L. Ten Years Venturing in ZnO Nanostructures: From Discovery to Scientific Understanding and to Technology Applications. *Chin. Sci. Bull.* **2009**, *54*, 4021−4034.

(5) Zeng, H.; Duan, G.; Li, Y.; Yang, S.; Xu, X.; Cai, W. Blue Luminescence of ZnO Nanoparticles Based on Non-equilibrium Processes: Defect Origins and Emission Controls. *Adv. Funct. Mater.* **2010**, *20*, 561−572.

(6) Baruah, S.; Dutta, J. Hydrothermal Growth of ZnO Nanostructures. *Sci. Technol. Adv. Mater.* **2009**, *10*, 013001.

(7) Johnson, J. C.; Yan, H.; Yang, P.; Saykally, R. J. Optical Cavity Effects in ZnO Nanowire Lasers and Waveguides. *J. Phys. Chem. B* **2003**, *107*, 8816−8828.

(8) Voss, T.; Svacha, G. T.; Mazur, E.; Müller, S.; Ronning, C.; Konjhodzic, D.; Marlow, F. High-Order Waveguide Modes in ZnO Nanowires. *Nano Lett.* **2007**, *7*, 3675−3680.

(9) Koch, M. H.; Timbrell, P.; Lamb, R. N. The Influence of Film Crystallinity on the Coupling Efficiency of ZnO Optical Modulator Waveguides. *Semicond. Sci. Technol.* **1995**, *10*, 1523.

(10) Baxter, J. B.; Walker, A.; Van Ommering, K.; Aydil, E. Synthesis and Characterization of ZnO Nanowires and their Integration into Dye-sensitized Solar Cells. *Nanotechnology* **2006**, *17*, S304.

(11) Cho, S.; Kim, S.; Jang, J.-W.; Jung, S.-H.; Oh, E.; Lee, B. R.; Lee, K.-H. Large-Scale Fabrication of Sub-20-nm-Diameter ZnO Nanorod Arrays at Room Temperature and Their Photocatalytic Activity. *J. Phys. Chem. C* **2009**, *113*, 10452−10458.

(12) Lupan, O.; Pauporté, T.; Le Bahers, T.; Ciofini, I.; Viana, B. High Aspect Ratio Ternary Zn_{1-x} Cd_x O Nanowires by Electrodeposition for Light-Emitting Diode Applications. *J. Phys. Chem. C* **2011**, *115*, 14548−14558.

(13) Lupan, O.; Emelchenko, G. A.; Ursaki, V. V.; Chai, G.; Redkin, A. N.; Gruzintsev, A. N.; Tiginyanu, I. M.; Chow, L.; Ono, L. K.; Roldan Cuenya, B. Synthesis and Characterization of ZnO Nanowires for Nanosensor Applications. *Mater. Res. Bull.* **2010**, *45*, 1026−1032.

(14) Xie, Y.; He, Y.; Irwin, P. L.; Jin, T.; Shi, X. Antibacterial Activity and Mechanism of Action of Zinc Oxide Nanoparticles Against *Campylobacter jejuni*. *Appl. Environ. Microbiol.* **2011**, *77*, 2325−2331.

(15) Mishra, Y. K.; Adelung, R.; Röhl, C.; Shukla, D.; Spors, F.; Tiwari, V. Virostatic Potential of Micro-nano Filopodia-like ZnO Structures Against Herpes Simplex Virus-1. *Antiviral Res.* **2011**, *92*, 305−312.

(16) Antoine, T.; Mishra, Y. K.; Trigilio, J.; Tiwari, V.; Adelung, R.; Shukla, D. Prophylactic, Therapeutic and Neutralizing Effects of Zinc Oxide Tetrapod Structures Against Herpes Simplex Virus Type-2 Infection. *Antiviral Res.* **2012**, *96*, 363−375.

(17) Wahab, R.; Dwivedi, S.; Umar, A.; Singh, S.; Hwang, I.; Shin, H.-S.; Musarrat, J.; Al-Khedhairy, A. A.; Kim, Y.-S. ZnO Nanoparticles Induce Oxidative Stress in Cloudman S91 Melanoma Cancer Cells. *J. Biomed. Nanotechnol.* **2013**, *9*, 441−449.

(18) Zhou, J.; Xu, N. S.; Wang, Z. L. Dissolving Behavior and Stability of ZnO Wires in Biofluids: A Study on Biodegradability and Biocompatibility of ZnO Nanostructures. *Adv. Mater.* **2006**, *18*, 2432−2435.

(19) Papavlassopoulos, H.; Mishra, Y. K.; Kaps, S.; Paulowicz, I.; Abdelaziz, R.; Elbahri, M.; Maser, E.; Adelung, R.; Röhl, C. Toxicity of Functional Nano-micro Zinc Oxide Tetrapods: Impact of Cell Culture Conditions, Cellular Age, and Material Properties. *PLoS One* **2014**, *9*, e84983.

(20) Tian, D.; Zhang, X.; Zhai, J.; Jiang, L. Photocontrollable Water Permeation on the Micro/nanoscale Hierarchical Structured ZnO Mesh Films. *Langmuir* **2011**, *27*, 4265−4270.

(21) Nobis, T.; Kaidashev, E. M.; Rahm, A.; Lorenz, M.; Grundmann, M. Whispering Gallery Modes in Nanosized Dielectric Resonators with Hexagonal Cross-section. *Phys. Rev. Lett.* **2004**, *93*, 103903.

(22) Zhang, Y.; Zhou, H.; Liu, S.; Tian, Z. R.; Xiao, M. Second-Harmonic Whispering-Gallery Modes in ZnO Nanotetrapod. *Nano Lett.* **2009**, *9*, 2109−2112.

(23) Gargas, D. J.; Moore, M. C.; Ni, A.; Chang, S.-W.; Zhang, Z.; Chuang, S.-L.; Yang, P. Whispering Gallery Mode Lasing from Zinc Oxide Hexagonal Nanodisks. *ACS Nano* **2010**, *4*, 3270−3276.

(24) Chen, R.; Ling, B.; Sun, X. W.; Sun, H. D. Room Temperature Excitonic Whispering Gallery Mode Lasing from High-Quality Hexagonal ZnO Microdisks. *Adv. Mater.* **2011**, *23*, 2199−2204.

(25) Ursaki, V. V.; Burlacu, A.; Rusu, E.; Postolake, V.; Tiginyanu, I. M. Whispering Gallery Modes and Random Lasing in ZnO Microstructures. *J. Opt. A: Pure Appl. Opt.* **2009**, *11*, 075001.

(26) Baruah, S.; Thanachayanont, C.; Dutta, J. Growth of ZnO Nanowires on Nonwoven Polyethylene Fibers. *Sci. Technol. Adv. Mater.* **2008**, *9*, 025009.

(27) Lupan, O.; Pauporté, T.; Le Bahers, T.; Viana, B.; Ciofini, I. Wavelength Emission Tuning of ZnO Nanowire Based Light Emitting Diodes by Cu Doping: Experimental and Computational Insights. *Adv. Funct. Mater.* **2011**, *21*, 3564−3572.

(28) Wagner, R. S.; Ellis, W. C. Vapor−Liquid−Solid Mechanism of Single Crystal Growth. *Appl. Phys. Lett.* **1964**, *4*, 89−90.

(29) Jebril, S.; Kuhlmann, H.; Müller, S.; Ronning, C.; Kienle, L.; Duppel, V.; Mishra, Y. K.; Adelung, R. Epitactically Interpenetrated High Quality ZnO Nanostructured Junctions on Microchips Grown by the Vapor−Liquid−Solid Method. *Cryst. Growth Des.* **2010**, *10*, 2842−2846.

(30) Menke, E. J.; Thompson, M. A.; Xiang, C.; Yang, L. C.; Penner, R. M. Lithographically Patterned Nanowire Electrodeposition. *Nat. Mater.* **2006**, *5*, 914−919.

(31) Lupan, O.; Pauporté, T.; Viana, B. Low-temperature Growth of ZnO Nanowire Arrays on p-Silicon (111) for Visible-Light-Emitting Diode Fabrication. *J. Phys. Chem. C* **2010**, *114*, 14781−14785.

(32) Ostrikov, K.; Neyts, E. C.; Meyyappan, M. Plasma Nanoscience: From Nano-solids in Plasmas to Nano-plasmas in Solids. *Adv. Phys.* **2013**, *62*, 113−224.

(33) Ostrikov, K.; Seo, D. H.; Mehdipour, H.; Cheng, Q.; Kumar, S. Plasma Effects in Semiconducting Nanowire Growth. *Nanoscale* **2012**, *4*, 1497−1508.
(34) Strobel, R.; Pratsinis, S. E. Flame Aerosol Synthesis of Smart Nanostructured Materials. *J. Mater. Chem.* **2007**, *17*, 4743−4756.
(35) Adelung, R.; Aktas, O. C.; Franc, J.; Biswas, A.; Kunz, R.; Elbahri, M.; Kanzow, J.; Schurmann, U.; Faupel, F. Strain-controlled Growth of Nanowires within Thin-film Cracks. *Nat. Mater.* **2004**, *3*, 375−379.
(36) Song, J.; Kulinich, S. A.; Yan, J.; Li, Z.; He, J.; Kan, C.; Zeng, H. Epitaxial ZnO Nanowire on Nanoplate Structures as Efficient and Transferable Field Emitters. *Adv. Mater.* **2013**, *25*, 5750−5755.
(37) Gedamu, D.; Paulowicz, I.; Kaps, S.; Lupan, O.; Wille, S.; Haidarschin, G.; Mishra, Y. K.; Adelung, R. Rapid Fabrication Technique for Interpenetrated ZnO Nanotetrapod Networks for Fast UV Sensors. *Adv. Mater.* **2014**, *26*, 1541−1550.
(38) Pachauri, V.; Vlandas, A.; Kern, K.; Balasubramanian, K. Site Specific Self-assembled Liquid-Gated ZnO Nanowire Transistors for Sensing Applications. *Small* **2010**, *6*, 589−594.
(39) Ladanov, M.; Algarin-Amaris, P.; Matthews, G.; Ram, M.; Thomas, S.; Kumar, A.; Wang, J. Microfluidic Hydrothermal Growth of ZnO Nanowires over High Aspect Ratio Microstructures. *Nanotechnology* **2013**, *24*, 375301.
(40) Mehare, R. S.; Devarapalli, R. R.; Yenchalwar, S. G.; Shelke, M. V. Microfluidic Spatial Growth of Vertically Aligned ZnO Nanostructures by Soft Lithography for Antireflective Patterning. *Microfluid. Nanofluid.* **2013**, *15*, 1−9.
(41) Mishra, Y. K.; Kaps, S.; Schuchardt, A.; Paulowicz, I.; Jin, X.; Gedamu, D.; Freitag, S.; Claus, M.; Wille, S.; Kovalev, A.; Gorb, S. N.; Adelung, R. Fabrication of Macroscopically Flexible and Highly Porous 3D Semiconductor Networks from Interpenetrating Nanostructures by a Simple Flame Transport Approach. *Part. Part. Syst. Charact.* **2013**, *30*, 775−783.
(42) Jin, X.; Götz, M.; Wille, S.; Mishra, Y. K.; Adelung, R.; Zollfrank, C. A Novel Concept for Self-Reporting Materials: Stress Sensitive Photoluminescence in ZnO Tetrapod Filled Elastomers. *Adv. Mater.* **2013**, *25*, 1342−1347.
(43) Chang, C.; Wang, Y.-F.; Kanamori, Y.; Shih, J.-J.; Kawai, Y.; Lee, C.-K.; Wu, K.-C.; Esashi, M. Etching Submicrometer Trenches by using the Bosch Process and its Application to the Fabrication of Antireflection Structures. *J. Micromech. Microeng.* **2005**, *15*, 580.
(44) Geburt, S.; Thielmann, A.; Röder, R.; Borschel, C.; McDonnell, A.; Kozlik, M.; Kühnel, J.; Sunter, K. A.; Capasso, F.; Ronning, C. Low Threshold Room-temperature Lasing of CdS Nanowires. *Nanotechnology* **2012**, *23*, 365204.
(45) Chan, E. P.; Smith, E. J.; Hayward, R. C.; Crosby, A. J. Surface Wrinkles for Smart Adhesion. *Adv. Mater.* **2008**, *20*, 711−716.
(46) Damen, T. C.; Porto, S. P. S.; Tell, B. Raman Effect in Zinc Oxide. *Phys. Rev.* **1966**, *142*, 570.
(47) Šćepanović, M.; Grujić-Brojčin, M.; Vojisavljević, K.; Bernik, S.; Srećković, T. Raman Study of Structural Disorder in ZnO Nanopowders. *J. Raman Spectrosc.* **2010**, *41*, 914−921.
(48) Ozgur, U.; Alivov, Y. I.; Liu, C.; Teke, A.; Reshchikov, M. A.; Dogan, S.; Avrutin, V. C. S. J.; Cho, S.-J.; Morkoc, H. A Comprehensive Review of ZnO Materials and Devices. *J. Appl. Phys.* **2005**, *98*, 041301−041301-103.
(49) Lupan, O.; Pauporté, T.; Chow, L.; Viana, B.; Pellé, F.; Ono, L. K.; Roldan Cuenya, B.; Heinrich, H. Effects of Annealing on Properties of ZnO Thin Films Prepared by Electrochemical Deposition in Chloride Medium. *Appl. Surf. Sci.* **2010**, *256*, 1895−1907.
(50) Wan, Q.; Wang, T. H.; Zhao, J. C. Enhanced Photocatalytic Activity of ZnO Nanotetrapods. *Appl. Phys. Lett.* **2005**, *87*, 083105.
(51) Jang, E. S.; Won, J. H.; Hwang, S. J.; Choy, J. H. Fine Tuning of the Face Orientation of ZnO Crystals to Optimize Their Photocatalytic Activity. *Adv. Mater.* **2006**, *18*, 3309−3312.
(52) Zheng, Y.; Chen, C.; Zhan, Y.; Lin, X.; Zheng, Q.; Wei, K.; Zhu, J.; Zhu, Y. Luminescence and Photocatalytic Activity of ZnO Nanocrystals: Correlation between Structure and Property. *Inorg. Chem.* **2007**, *46*, 6675−6682.
(53) Sun, T.; Qiu, J.; Liang, C. Controllable Fabrication and Photocatalytic Activity of ZnO Nanobelt Arrays. *J. Phys. Chem. C* **2007**, *112*, 715−721.
(54) Wang, Y.; Li, X.; Wang, N.; Quan, X.; Chen, Y. Controllable Synthesis of ZnO Nanoflowers and their Morphology-Dependent Photocatalytic Activities. *Sep. Purif. Technol.* **2008**, *62*, 727−732.
(55) McLaren, A.; Valdes-Solis, T.; Li, G.; Tsang, S. C. Shape and Size Effects of ZnO Nanocrystals on Photocatalytic Activity. *J. Am. Chem. Soc.* **2009**, *131*, 12540−12541.
(56) Ruiz Peralta, M. D. L.; Pal, U.; Zeferino, R. S. Photoluminescence (PL) Quenching and Enhanced Photocatalytic Activity of Au-Decorated ZnO Nanorods Fabricated through Microwave-Assisted Chemical Synthesis. *ACS Appl. Mater. Interfaces* **2012**, *4*, 4807−4816.
(57) Leelavathi, A.; Madras, G.; Ravishankar, N. Origin of Enhanced Photocatalytic Activity and Photoconduction in High Aspect Ratio ZnO Nanorods. *Phys. Chem. Chem. Phys.* **2013**, *15*, 10795−10802.
(58) Pyne, S.; Sahoo, G. P.; Bhui, D. K.; Bar, H.; Sarkar, P.; Samanta, S.; Maity, A.; Misra, A. Enhanced Photocatalytic Activity of Metal-Coated ZnO Nanowires. *Spectrochimica Acta Part A: Mol. Biomol. Spectros.* **2012**, *93*, 100−105.
(59) Ma, C.; Zhou, Z.; Wei, H.; Yang, Z.; Wang, Z.; Zhang, Y. Rapid Large-scale Preparation of ZnO Nanowires for Photocatalytic Application. *Nanoscale Res. Lett.* **2011**, *6*, 1−5.